FABRICATION AND TESTING OF PROTON PRECESSION MAGNETOMETER FOR MEASUREMENT OF EARTH MAGNETIC FIELD ANOMALY

AYANDA, J.D., OGUNSANWO, F.O.*, OLABAMIJI, P. AND FALAYI, E.O.
Department of Physics, Tai Solarin University of Education, Nigeria

ABSTRACT
A Proton Precession Magnetometer (PPM) was fabricated and configured with a portable P.C. for the geomagnetic field measurements. It has sensors made of copper coil, SWG 28, coiled into 4 layers of about 4000 turns wound on two bottles filled with a proton-rich distilled water, placed at right angles to the ambient magnetic field. A strong current energizes the coil, creating a strong polarization field, which orientates all the protons of the fluid in the same direction and stops their precession. When the polarization current is sharply ended, all the protons resume their normal precession but now, in phase and thus the accumulated actions of these small magnets induces a small audio sine wave signal. The PPM constructed on Printed Circuit Board (PCB) and with sensor, were housed separately in two impact resistance plastic case, with a total weight of 5 kg and configured with external sound card of a computer. The Fabricated PPM (FPPM) and Standard PPM (SPPM) were used simultaneously for field measurements at a selected test site of five traverses T_1, T_2, T_3, T_4 and T_5. Graphs and contour maps were drawn from data acquired using FPPM and SPPM, for the analysis. The FPPM was found to be reliable for geomagnetic survey measurements with correlation values ranged between 0.56 – 0.88. The developed coded equipment fabricated locally will make it easily repairable when this equipment develop fault.

Keywords: contour map, fabricated, magnetic intensity, magnetometer, precession, residual
***Correspondence:** godif07@yahoo.com, 07069302863

INTRODUCTION

In everyday life, magnetic fields are most often encountered as a force created by permanent magnetic materials such as iron, cobalt, or nickel, and attract or repel other magnets. They are widely used in modern technology, particularly in electrical engineering and electro-mechanics in electric motors, and dynamos [1 – 3]. The earth produces its own magnetic field, which is important for navigation, and also shields the earth's atmosphere from solar wind [4 – 7]. The origin of the earth main magnetic field is explained by the 'Dynamo's theory' as a self-existing (or self-sustaining) dynamo (Figure 1).

The magnitude of the magnetic field of a current caring conductor at a vector space $\hat{r}$ to the conductor by Biot-Savart law is given in equation (1) specified by Isholaet *al.* [8] and Kayodeet *al.* [9].

$$d\vec{B} = \frac{\mu_o}{4\pi}\frac{Id\vec{l}\times\hat{r}}{r^2} \qquad (1)$$

To measure the intensity of earth magnetic field a magnetometer is required, a magnetometer is an instrument used to measure the relative change in direction and strength of a magnetic field at a particular location, expressed in nano Tesla (nT) or gamma (1nT=1gamma).

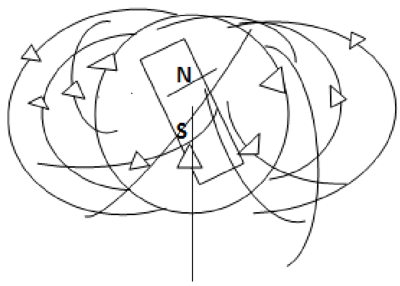

Figure 1: The Earth's Magnetic Field

There are now a number of portable magnetometers based on different physical principles, namely: Fluxgate magnetometer, Proton Precession Magnetometer, An 'Overhauser' PPM and Cesium Magnetometer. The first attempt to measure magnetic intensity using magnetometer was by Carl Friedric Gauss in 1833. Francis Ronald and Charles Brooke independently invented magnetograph in 1846, which continuously recorded the magnets movements using photography. The oldest magnetic prospecting instrument is the magnetic compass, which measures the field direction. Other instruments include magnetic balances and fluxgate magnetometers. Most magnetic surveys are made with proton-precession or optical-pumping magnetometers, which are appreciably more accurate. The proton magnetometer measures a radio-frequency voltage induced in a coil by the reorientation (precession) of magnetically polarized protons in a container of water while the optical- pumping magnetometer makes use of the principles of nuclear resonance and cesium or rubidium vapour [10, 11]. It can detect minute magnetic fluctuations.

Proton Precession Magnetometer is a scalar magnetometer used for measurement of the Earth's magnetic field amplitude [12 – 15]. It consists of a proton-rich fluid (commonly hydrogen or kerosene) in a container, surrounded by a coil. When current is passed through the coil, a magnetic field is induced and the protons in the fluid align themselves with the magnetic field. When the current is turned off, the protons re-align themselves with the Earth's magnetic field resulting in a precession frequency which is directly proportional to the external magnetic field with a resolution of 0.1 nT, while accuracies of 0.5 nT are achievable in the field [16, 17]. The precession protons then generate a small induced e. m. f whose frequency is precisely proportional to the total earth's magnetic field given in equation (2) by [18, 19] as

$$\vec{B} = \frac{2\pi\ f}{r} \quad (2)$$

where,

B = total field intensity, f = frequency of precession, r = gyromagnetic ratio with a fundamental constant value of $2.675222005 \times 10^{8}$ rads^{-1}T^{-1}.

By precisely measuring precession frequency of protons, earth's magnetic field can be measured. This precession frequency band ranges between 1KHz to 3KHz [20, 21].

A major problem that needs to be considered in designing a sensor coil is the environmental noise as this noise is picked up by the sensor coil, and the actual geomagnetic signal information picked up by the sensor in form of sinusoidal variations of proton precession is extremely weak in amplitude and last for few seconds, while the polarization circuit and signal conditioning circuit should be isolated from each other to avoid noise loop formation [22]. The magnetic anomalies present in Earth's crust and its interior create magnetic gradients in geomagnetic field being measured, thus distorting it, and making the signal to decay faster than normal.

The following vector fields are required for the determination of electric field and magnetic field within a given region, namely: (i) Electric field intensity , E (volt/m) (ii) Magnetic flux density or magnetic induction B, (weber/m = Tesla) (iii) Magnetic field intensity H, (A/m) (iv) The displacement current density, D (coulomb/m) (v) Current density, J, (A/m^2)

The vector fields are related by Maxwell's equation as reported by [23 - 27]:

$$\nabla \times \hat{E} = \frac{-\partial \hat{B}}{\partial t} = -\mu \frac{d\hat{H}}{dt} \quad (3)$$

Since B=μH

$$\nabla \times \hat{H} = J + \frac{\partial \hat{D}}{\partial t} \quad (4)$$

Let us define a vector magnetic potential (A) in terms of flux density, B, such that

$$\nabla \times A = \hat{B} \quad (5)$$

Relating equation (5) to equation (3), we have

$$\frac{\partial}{\partial t}(\nabla \times A) = \frac{\partial \hat{B}}{\partial t} \quad (6)$$

$$\frac{-\partial}{\partial t}(\nabla \times A) = \frac{-\partial \hat{B}}{\partial t}$$

Hence putting equation (6) into equation (3) we have

$$\frac{-\partial}{\partial t}(\nabla \times A) = \nabla \times \hat{E}$$

$$\nabla \times \frac{-\partial A}{\partial t} = \nabla \times \hat{E} \quad (7)$$

$$\hat{E} = \frac{-\partial A}{\partial t}$$

Taking the curl of equation (5), we have

$$\nabla \times \nabla \times A = \nabla \times B$$

But $\nabla \times \nabla \times A = \nabla(\nabla . A) - \nabla . \nabla A$

$$= 0 - \nabla . \nabla A \quad (8)$$

$$= -\nabla^2 A$$

But $\nabla . A = 0$

Hence, $\nabla \times \nabla \times A = -\nabla^2 A$

$$\therefore \nabla^2 A = -\nabla \times B$$

(9)

But $B = \mu H$

$$\nabla^2 A = -\nabla \times \mu \hat{H}$$
$$= -\mu(\nabla \times \hat{H})$$
$$\nabla^2 A = -\mu\left\{ J + \frac{\partial \hat{D}}{\partial t} \right\} \quad (10)$$

$\sigma = \frac{1}{\ell}$ resistance

D= εE

But $J = \frac{E}{\ell} = \sigma E$

σ =conductivity

E=electric permittivity

$$\nabla^2 A = -\mu\sigma\hat{E} - \mu\varepsilon \frac{\partial \hat{E}}{\partial t} \quad (11)$$

The second term of the R.H.S tends to zero since I_o is small.

$$\therefore \nabla^2 A = \mu\sigma \frac{\partial A}{\partial t}\left[\frac{\partial A}{\partial t} = -E \right] \quad (12)$$

$$= -\mu\sigma E$$
$$(Y = \sigma E)\nabla^2 A = -\mu y$$

(13)

Equation (13) is similar to the Poisson equation in magnetic and gravity and has a solution of the form

$$A = \frac{\mu}{4\pi\delta vol} \frac{Jdr}{r} \quad (14)$$

$$r = \sqrt{x^2 + y^2 + z^2}$$

where dr = Volume differential

The magnetic field at the centre of the magnetometer circular coils of radius r with N turns is given as;

$$\partial H_C = \frac{Ids \sin\theta}{4\pi r^2} = \partial H \quad (15)$$

Since sin90 =1

$$H_C = \int_0^{2\pi r} \frac{Ids}{4\pi r^2} I . \frac{2\pi r}{4\pi r^2}$$

$$= \frac{I}{4\pi r^2}\left[S \right]_0^{2\Pi r} = \frac{I.2\pi r}{4\pi r^2} = \frac{I}{2r}$$

For N-turns

$$H_C = \frac{NI}{2r} \quad (16)$$

Based on the magnetic theory, this study therefore fabricated a proton precision magnetometer and its efficiency was examined by subjecting it to field survey test with a standard proton precision magnetometer and the results obtained along the five traverses were used for depth or thickness estimation.

MATERIALS AND METHODS

Design and Fabrication Procedures

The basic experimental arrangement of proton precession magnetometer is shown in the block diagram (Figure 2), which consists of a magnetic field sensor made of a coil of copper wire wounded around a container filled with a proton rich material, in this case, distilled water. This was followed by polarizing and energy dissipation handling circuits made up of microcontroller and electrical relays, followed by amplifiers and band pass filters circuits. The signal was digitized using the sound card of a computer, while the frequency of the detected signal was determined using Fourier analysis.

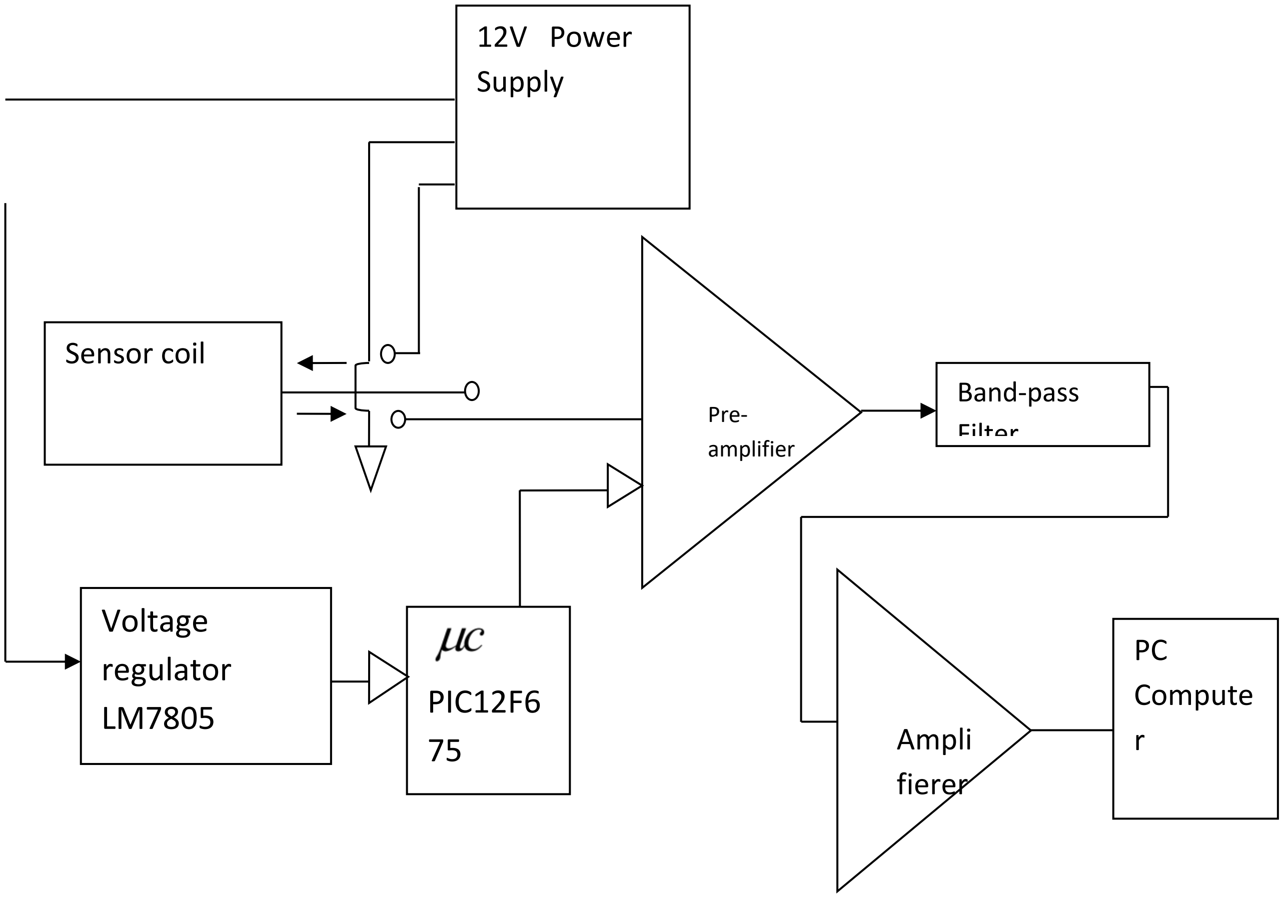

Figure 2: Functional blocks of the proton magnetometer

Sensor

In constructing the proton precession magnetometer, a sensor which consists of a coil of copper wire wounded around a container filled with a proton rich material such as water was used (Figure 3). A dual solenoid configuration was selected due to its property of cancellation of noise generated outside the coil. In this configuration, two identical single coil sensors were placed side by side for sensing the same magnetic field. The coils are connected in series so that the signals generated inside them are added together. In this arrangement, any noise induced in the two coils due to external sources will be canceled. Two plastic bottles having a diameter of 6.5cm and coil woundable section of 8.5cm were used as the containers. Plastic and glass have been reported to be suitable material for the containers being nonmagnetic and do not alter the local geomagnetic field. While water, benzene, kerosene is suitable as the proton rich samples, double distilled water was used due to its low cost and ease of use. The other reason for the use of water was its absence of reaction with plastic. The induced r.m.s signal voltage from a practical sensor is in the order of micro volts. To add to this problem, is the Johnson noise generated due to the finite resistance of the sensor.

Figure 3: The Sensor

Hence, it is important that the sensor has good signal to noise ratio for a given bandwidth of the band-pass filter. For a dual solenoid, the sensor constructed with identical containers of radius r_c length b wound with n turns of wire of resistivity ρ in l_s number of layers the induced r.m.s proton precession signal. The induced r.m.s signal voltage (V_{rms}) is given in equation (17) as designed by [29 - 31]:

$$V_{rms} = \eta_{\sin gle} \frac{\chi \omega_L \mu_o \eta_m n E \pi r_c^2 r_w^2 \sin \alpha}{2\sqrt{2} b \rho (r_c + r_w l_s)} \quad (17)$$

where, χ is the nuclear paramagnetic susceptibility of the proton rich materials used, μ_o is the magnetic permeability of free space, E is the voltage o f the polarizing supply used, ω_L is the Larmor precession angular frequency of the proton precession signal and α is the angle between the local geomagnetic field and the axis of the sensor.

η_m (filing factor) is a factor introduced to account for the inequality of the polarizing field throughout the entire cross section of the sensor.

$$\eta_m = \exp(-1.4 r_c / b) \quad (18)$$

We have introduced an additional factor $\eta_{single}$to account for the more fringing of the dual solenoid sensor when compared with its singles solenoid counterpart.

The signal to noise ratio (SNR) is presented in equation (19) as given by Parasnis [32] and Kohler [10];

$$SNR = \eta_{\sin gle} \frac{\chi \omega_L \mu_o \eta_m \sqrt{n} E \pi r_c^2 r_w^3 \sin \alpha}{2b\left[\left(r_c + r_w l_s\right)\rho\right]^{3/2} \sqrt{19.2 K \Delta T}} \qquad (19)$$

where K is the Boltzman constant and Δ T is the temperature of the sensor fluid.

Polarizing and Energy dissipation handling circuit

Normally, proton particles contained in fluids turn around their main axis but this axis also oscillates at a slower precession speed (a spinning top shows this v very clearly) whose value uniquely depends on the value of the ambient magnetic field [33, 34]. In a normal status, the precession movement is not synchronized between protons and thus has a canceling effect. A sensor filled with a proton-rich fluid is placed in a coil at right angles to the ambient magnetic field and a strong current energizes the coil, creating a strong magnetic field called polarization field, this orientates all the protons of the fluid in the same direction and stops their precession. When the polarization current is sharply ended, all the protons resume their normal precession but now, in phase and thus, the accumulated action of all these very small magnets induces a very small (at the µVolt RMS level) audio frequency Sine Wave signal in a signal pick-up coil (which could be the same as the polarization coil). This sine wave signal has a frequency depending only on the total value of the local magnetic field vector and lasts a few seconds (the relaxation time) during which the precession of the protons still stays in phase. This frequency is called the'Larmor' frequency. This voltage is amplified and its frequency precisely measured to determine the ambient field strength.

The exact relationship between ambient magnetic field (B in nT) and Larmor frequency (f) is given in equation (20) by Peter [33]:

$$B = \frac{f \times 100{,}000 \times 2 \times \pi}{26751.2} = f \times 23.4875 \qquad (20)$$

For example, for an average ambient field of 50,000nT, f will then be 2.128 KHz [17].

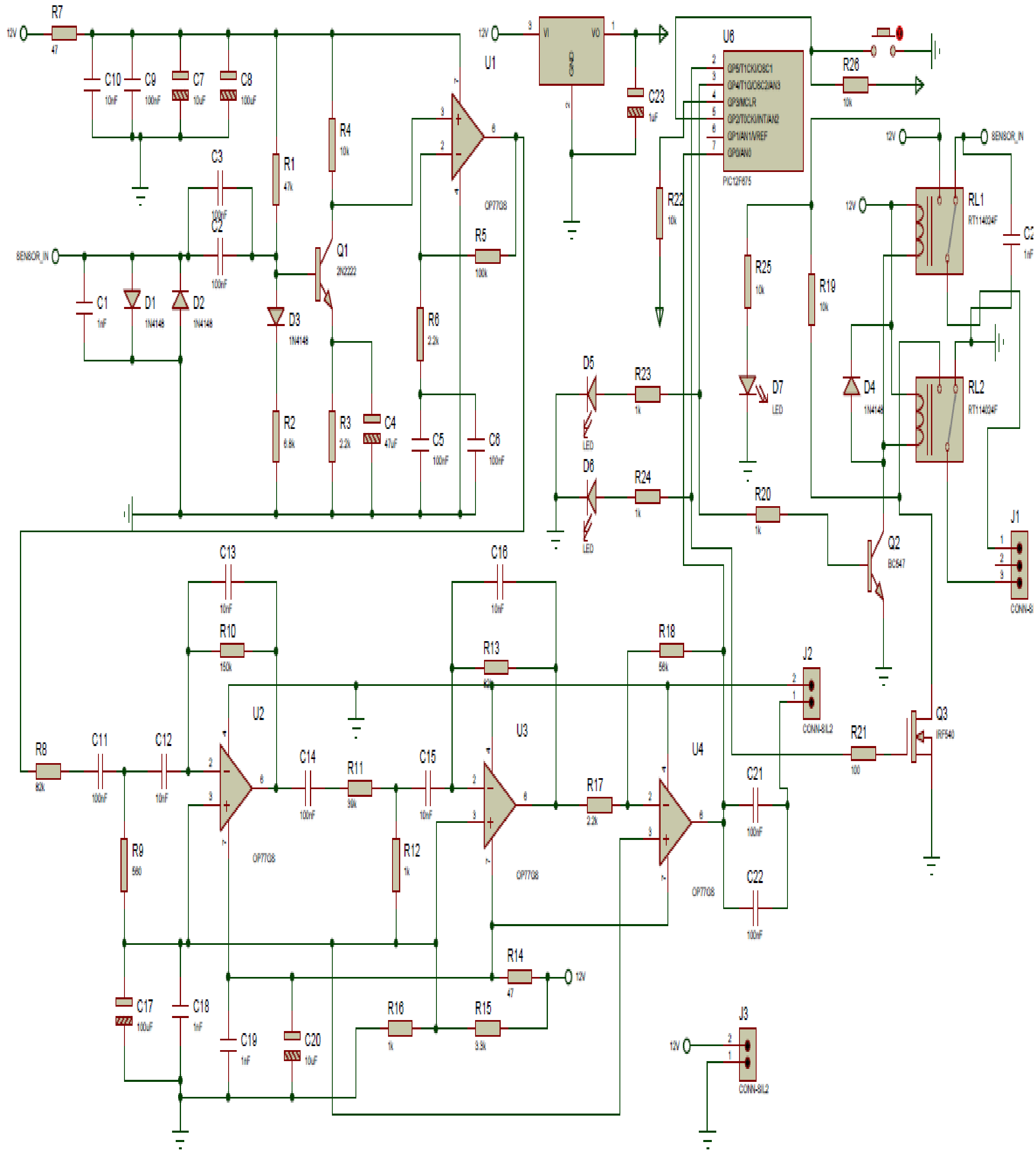

Figure 4: Circuit diagram of proton precession magnetometer [30]

RESULTS AND DISCUSSION

Circuit layout and coupled/ constructed PPM Result

Figures 5 shows the copper track patterns and the components layout on the printed circuit board diagram of the proton precession magnetometer, while Figure 6shows the constructed electronics panel board of the signal processing unit of the PPM. The computer oscilloscope of the PPM which displays the frequency of the magnetic field was presented in Figure 7 while Plate 1 depicts the FPPM arrangement.

The fabricated PPM was subjected to reliability field survey tests in conjunction with standard PPM a location along Ajibode road, University of Ibadan with a total of five traverses. For the analysis of the result graphs and maps were plotted namely:

(i) Ten different graphs for total magnetic intensity in (nT) against traverse points in (m) for both standard and fabricated magnetometer.

(ii) Ten graphs for residual anomaly in (nT) against traverse points in (m).

(iii) Contour maps for total magnetic intensity for both standard and fabricated magnetometer,

(iv) Residual contour maps for standard and fabricated PPM,

(v) Surface maps of magnetic intensity for standard and fabricated PPM, and

(vi) 3D wire frame maps of residual for standard and fabricated PPM.

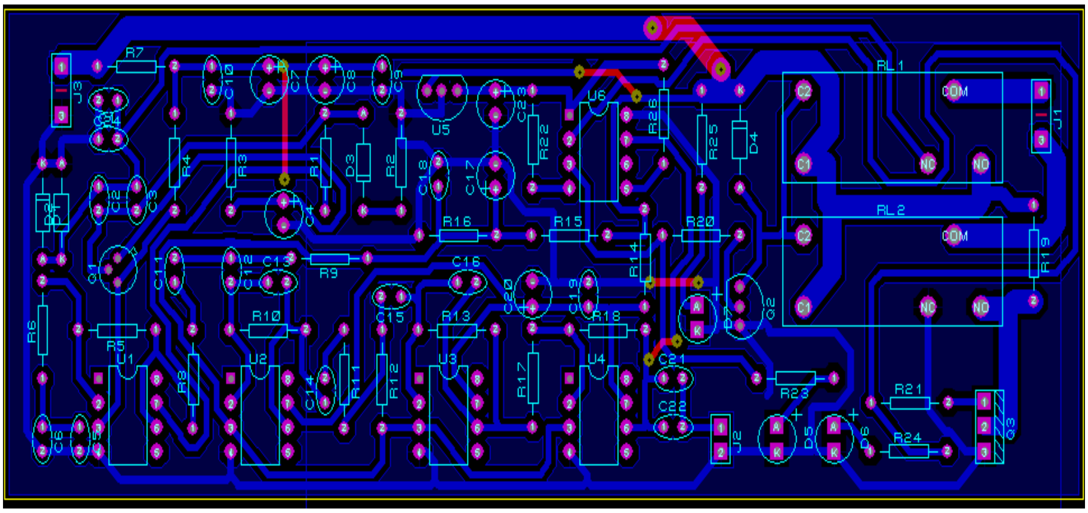

Figure 5: The Proteus Printed Circuit Board of PPM

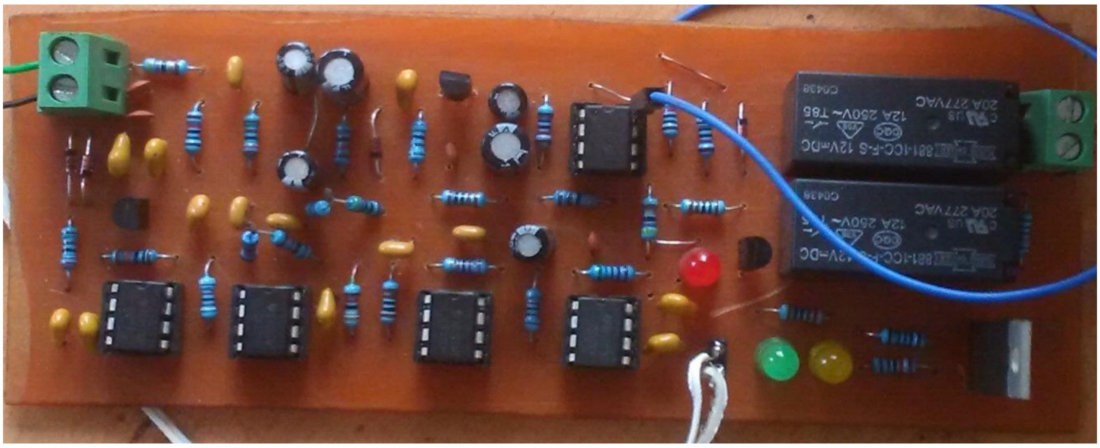

Figure 6: The Constructed circuit Board of the Signal Processing Unit of the PPM

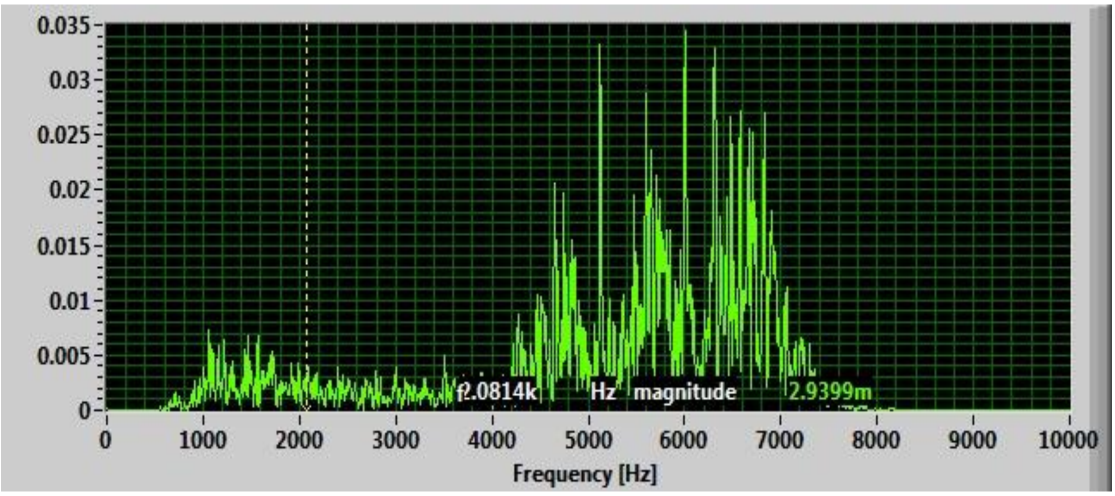

Figure 7: Computer Oscilloscope of the PPM the magnetic field frequency display

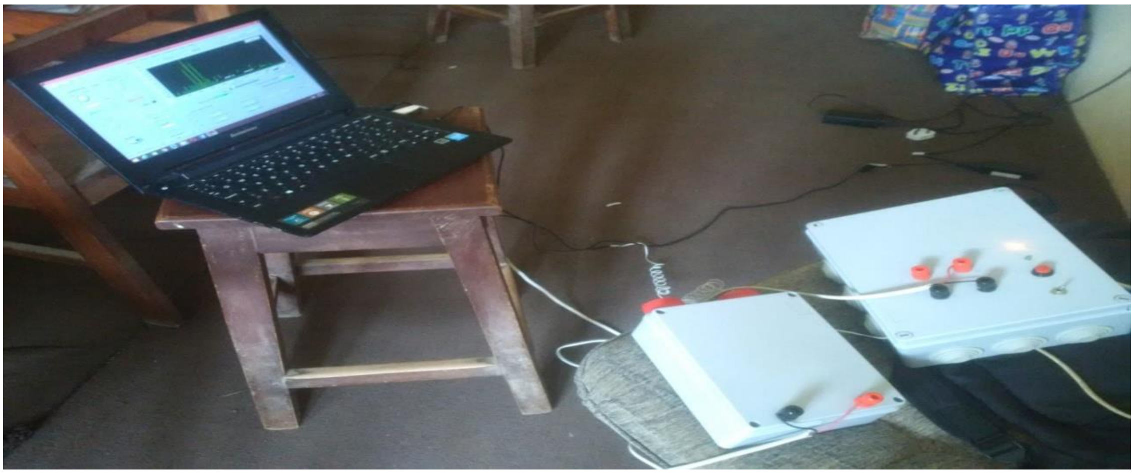

Plate 1: Picture of the Fabricated Proton Magnetometer arrangement.

The total magnetic field intensity, residual anomaly and comparative correlation of the standard and fabricated PPM

The profiles below for fabricated and standard were obtained from the relation given by Ogunsanwo *et al.* [35] in equation (21) as:

$$R = T - Z \quad (21)$$

where: R = residual magnetic anomaly

T = total magnetic intensity

Z = regional magnetic anomaly.

The qualitative and quantitative analysis of the magnetic survey depend on the computed magnetic anomaly data which was extracted from the total magnetic profile (Figures 8a and b) of both standard and fabricated magnetometer. For residual analysis, traverse 1 profile was shown to range between -20 to 3nT for fabricated (Figure 9a), and -60 to -4nT for standard (Figure 9b). In traverse 2, the residual profile was reported to range from -30 to 100 nT for standard, and 5 to 35 nT for Fabricated. Traverse 3, as well notice the amplitude of the residual profile ranging from -100 to 1 nT for Standard, and 0 to 70 nT for fabricated. In traverse 4, the residual profile of standard ranges from -400 to 600 nT , and that of fabricated is from -45 to -3 nT . In traverse 5, the residual profile for standard magnetometer is observed to range from -1300 to 100 nT, and -10 to 11 nT for the Fabricated proton magnetometer. The correlation result obtained for traverses 1 – 5 shows that the two surveys result are comparable with correlation coefficient ranged from 0.56 – 0.89 (Figure 10).

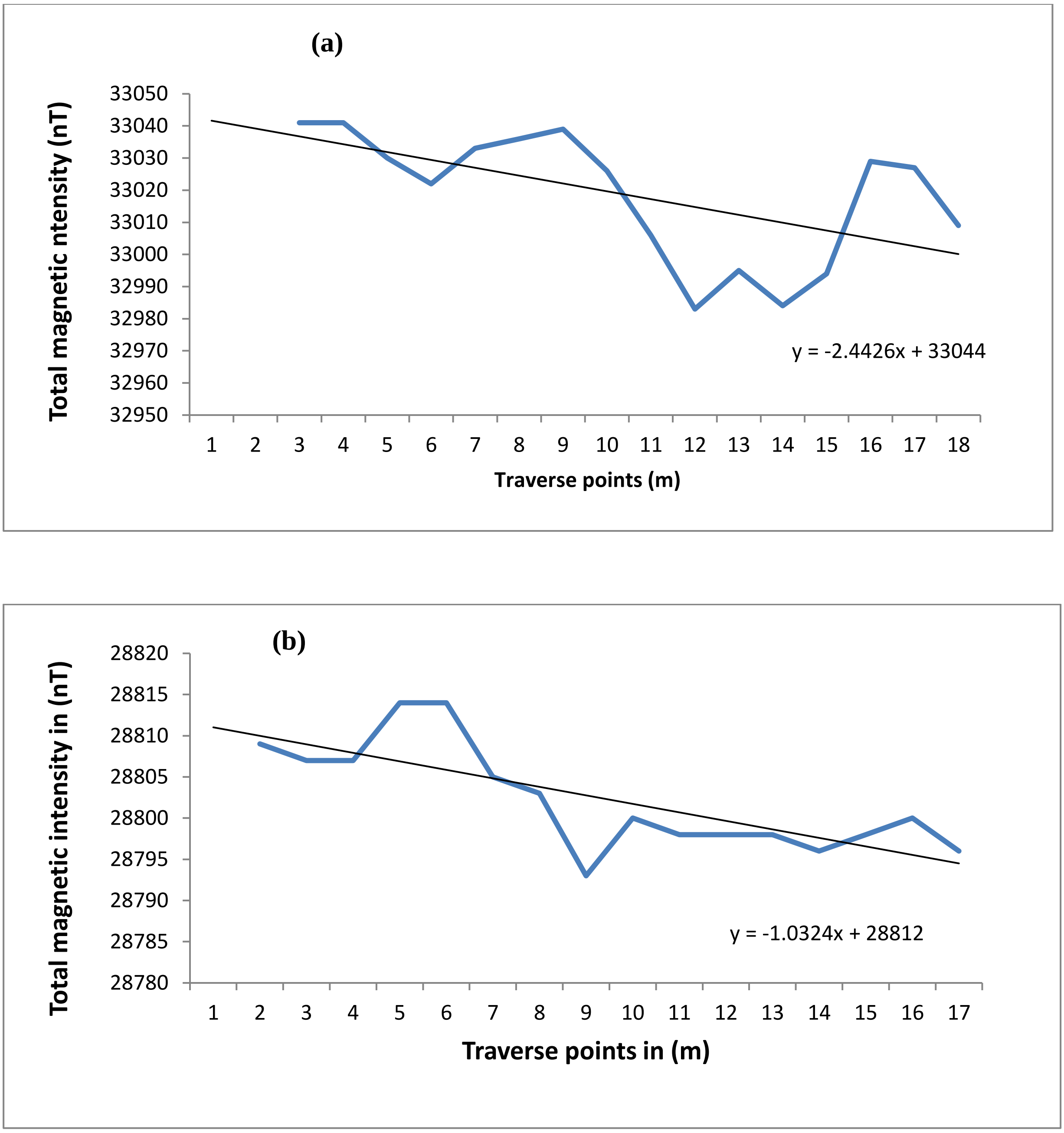

Figure 8: The graph of total magnetic intensity in (nT) against Travers points for **(a)** standard and **(b)** fabricated magnetometer

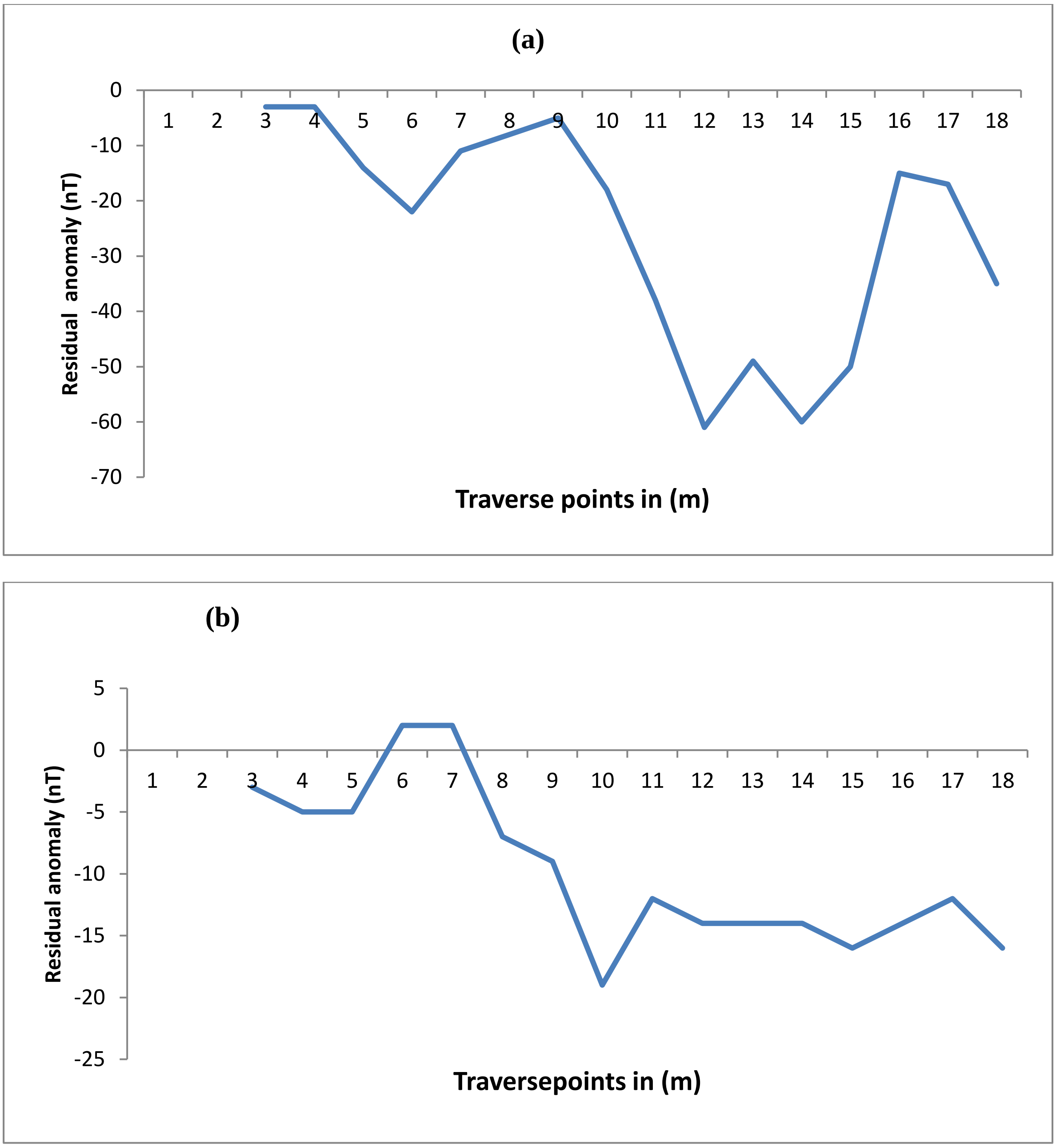

Figure 9: The graph of residual magnetic anomaly (nT) against Traverse points for **(a)**standard and **(b)** fabricated magnetometer

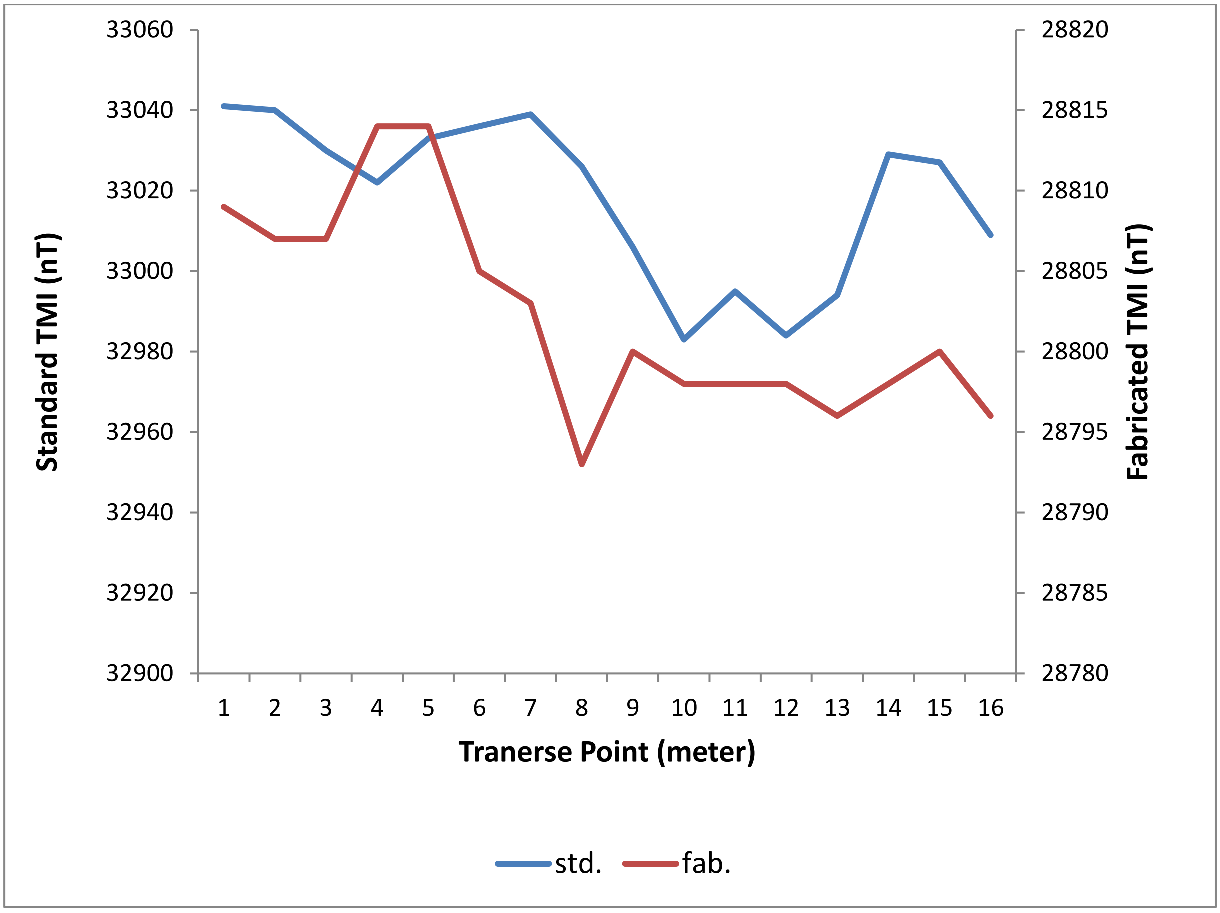

	std.	fab.
std.	1	
fab.	0.557543	1

Figure 10: Graph showing correlation between Standard and Fabricated magnetic intensity for traverse 1.

Contour, surface and wire frame naps

In this study, the magnetic survey results were subjected to spatial distribution using the contour, surface and wire map for anomaly identification. For standard contour maps, it was ranged from the region of higher magnetic intensity with the colour purple, while the least magnetic intensity was indicated with colour blue in Figure 11a. Likewise in fabricated, we have blue colour to denote the peak of the magnetic intensity, and the low intensity in orange colour as shown in Figure 11b. The residual contour map for the two PPM was presented in Figure 12. The magnetic peak region of standard PPM is denoted with white colour (Figure 12a), while the least intensity is in black colour. In the fabricated PPM (Figure 12b), we have color purple to show the peak of the magnetic intensity and the least intensity is in black. The peak region of the surface map as shown in Figures (13a and b) in colour blue for the standard PPM at about 33800nT as the region of highest magnetic intensity, while the red colour denote the peak of the magnetic intensity of the surface map for the fabricated machine at about 28905nT. This wire frames displays the depth to which the PPM can process in a particular region (residual) in Figure 14. For the standard PPM in Figure (14a) , we have the estimated depth in the range of 0 to 500m, while that of the fabricated PPM (Figure14b) was found in the range of -50 to 50 m.

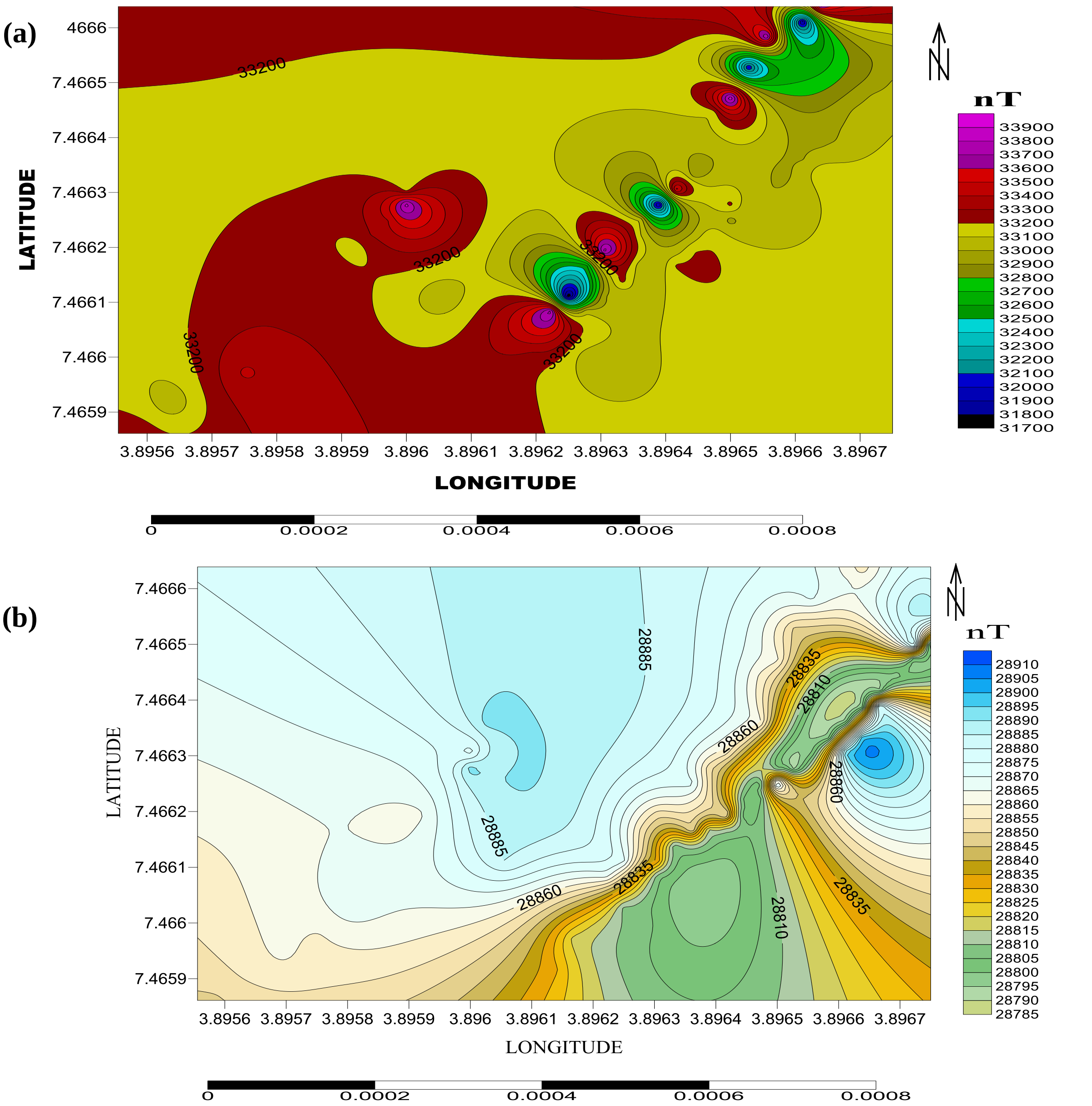

Figure 11: Contour map of Total magnetic intensity **(a)** Standard and **(b)** Fabricated

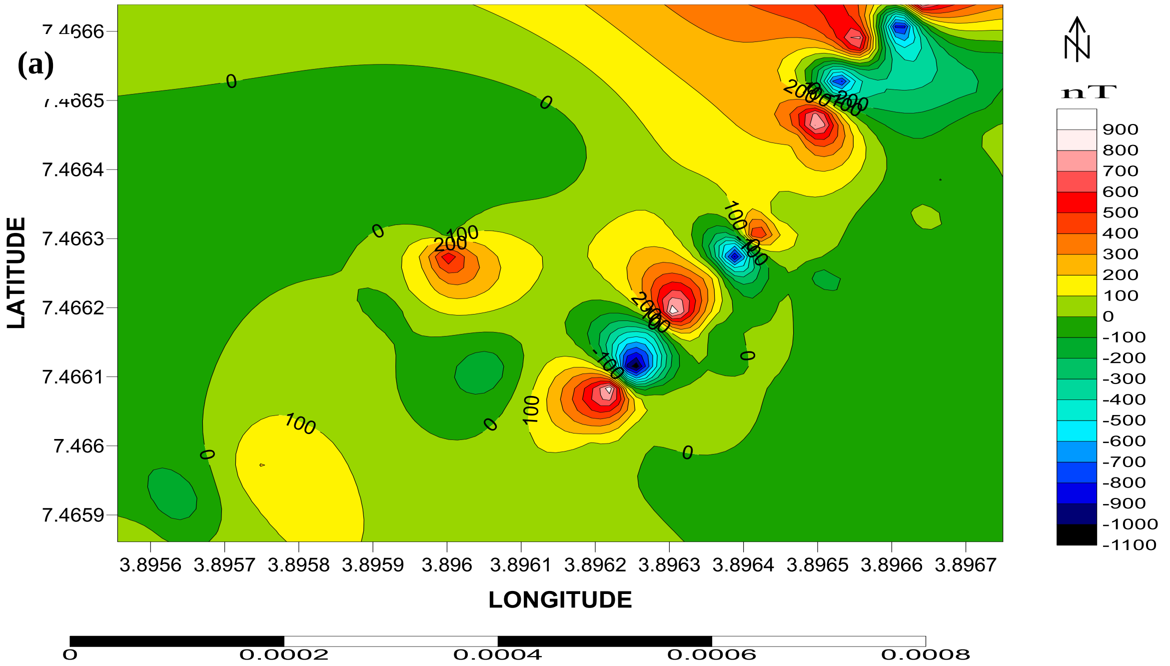

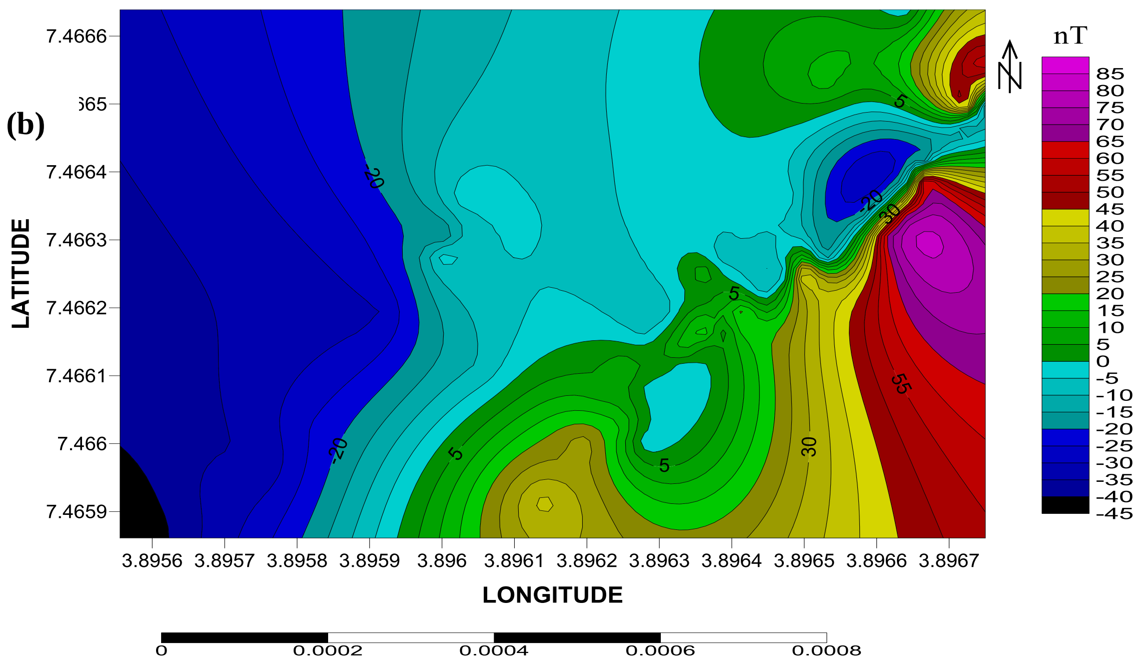

Figure 12: The Residual anomalous contour map for **(a)** Standard and **(b)** Fabricated

(a)

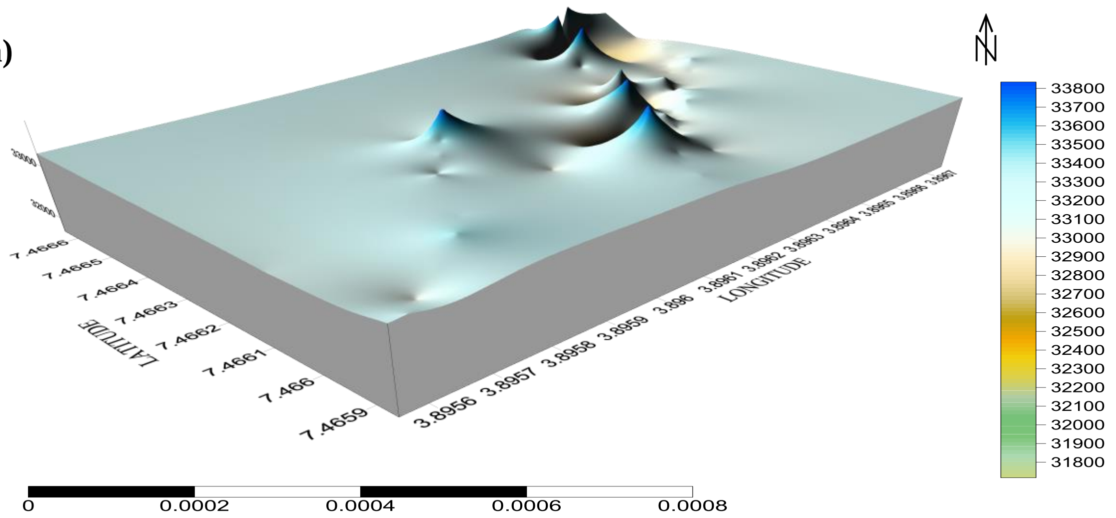

(b)

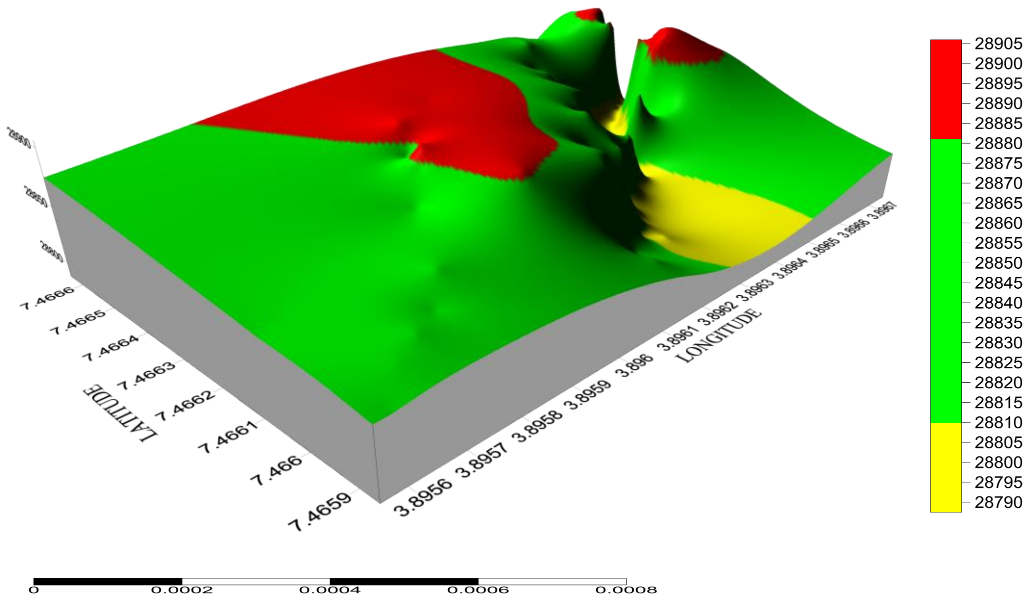

Figure 13: Surface map for Total magnetic intensity for **(a)** Standard and **(b)** Fabricated

(a)

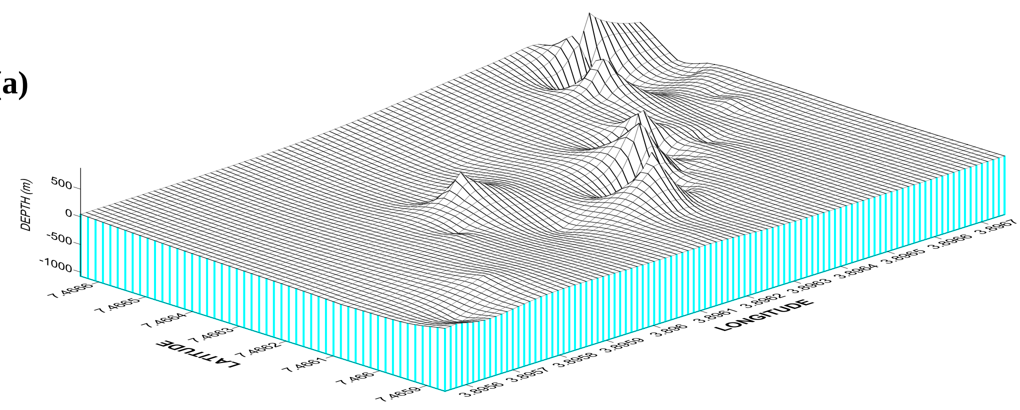

(b)

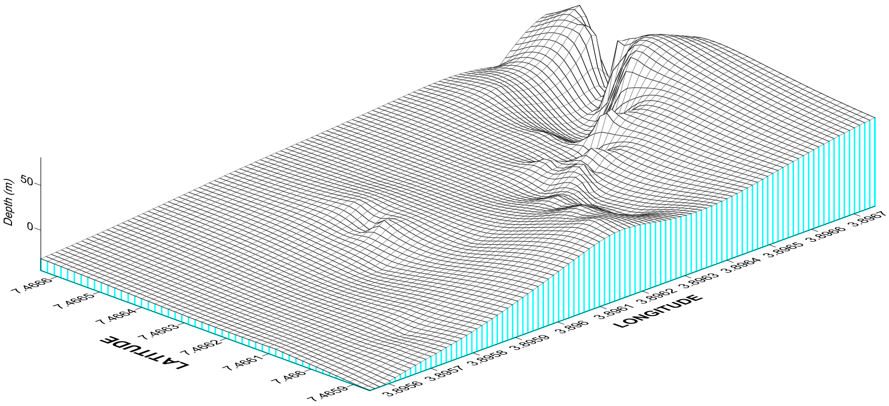

Figure 14: 3Dresidual wireframe map of (a) standard (b) fabricated of the study area

Table 1: The result collected for three layers indicating the thin body, intermediate thickness, and thick body for the 5 traverses.

TRAVERSES	STANDARD DEPTH (m)	FABRICATED DEPTH (m)	DIFFERENCES (m)
1	Thin body 7.25	Thin body 8.75	-1.50
	Intermediate thickness 5.44 m	Intermediate thickness 6.56 m	-1.12
	Thick body 4.35	Thick body 5.25	-0.90
2	Thin body 9.25	Thin body 8.25	1.00
	Intermediate thickness 6.94	Intermediate thickness 6.19	0.75
	Thick body 5.55	Thick body 4.95	0.60
3	Thin body 7.00	Thin body 4.50	2.50
	Intermediate thickness 5.25	Intermediate thickness 3.38	1.87
	Thick body 4.20	Thick body 2.70	1.50
4	Thin body 8.75	Thin body 8.00	0.75
	Intermediate thickness 6.56	Intermediate thickness 6.00	0.56
	Thick body 5.25	Thick body 4.80	0.45
5	Thin body 4.00	Thin body 7.25	-3.25
	Intermediate thickness 2.50	Intermediate thickness 4.53	-2.03

Thick body 2.40	Thick body 2.27	0.13

3.4 DISCUSSION

The specification of the proton precession magnetometer includes: A sensor(with specification given as: Copper coil of gauge given as SWG 28), coiled into 4 layers of about 4000turns for the two bottles with a coil wound length of 8.5cm for each container, diameter of each bottle given as 6.5cm, dc resistance of the coil- 12.4Ω, inductance of the coil- 55.4mH with a polarising current of about 0.48A for 12V supply and a RMS signal amplitude of 0.54µV.The signal to noise ratio(SNR) for bandwidth of 250 Hz is estimated as 61DB maximum, while the resonant capacitor for a precession frequency of 1715Hz equal to 0.8µF. The PPM has processing unit comprising of the following circuits namely: Polarizing and energy dissipation handling circuit, Pre amplifier circuit, band pass filter circuit, amplifier circuit and the display. The standard proton magnetometer contour maps range from the region of higher magnetic intensity with the colour purple, with values 33600 to 33900 nT while the least magnetic intensity is indicated with blue colour with values from 32900 to 33200nT (Figure 11a). Likewise, the fabricated proton magnetometer has blue colour to denote the peak of its magnetic intensity, 28900 to 28910 nT) and the least is denoted with orange colour (Figure 11b). The above enumerated magnetic intensity represents the total magnetic fields pick up at the traverses by the magnetometer which are embedded with noise.

The dominant magnetic field intensity from the residual (filtered magnetic field) contour map of the standard proton precession magnetometer (PPM) profile lies in the western part of the traverse, it ranges between -200 to 100 nT (Figure 12a), while the peak of its magnetic intensity on the eastern part of the traverse is at 900nT and the least is 1100 nT. These values are comparable with dominant magnetic field intensity from the residual contour map of the fabricated magnetometer, the western part shows low magnetic intensity between -45 to -5 nT (Fig. 12b), while a reasonably high magnetic intensity can be seen at the eastern path of the contour map given as 85nT.

The peak region of the surface map was color blue (Figure 13a) for the standard PPM at about 33800 nT denote the region of highest magnetic intensity, while the red colour (Figure 13b) denote the peak of the magnetic intensity of the surface map for the fabricated magnetometer at about 28905 nT. The wire frames display the depth to which the proton precession magnetometer (PPM) can delineate in a particular region. For the residual wire frame map, the depth of the anomaly found using the standard magnetometer is at about 0 to 500 m (Figure 14a), while for fabricated profile is at about -50 to 50m (Figure 14b). The depth and thickness of the survey area was estimated using peter half slope method and the result obtained was presented in Table 1 for the five traverses. The depth were estimated in the range of 4.35 – 7.25 m and 5.25 – 8.75 m for standard and fabricated meter; 5.55 – 9.25m and 4.95 – 8.25 m for standard and fabricated meter; 4.20 – 7.00 m and 2.70 – 4.50 m for standard and fabricated meter; 5.25 – 8.75 m and 4.80 – 8.00 m for standard and fabricated meter; 2.40 – 4.00 m and 2.70 – 7.25 m for standard and fabricated meter, for traverse 1, 2, 3, 4 and 5, respectively. The depth was computed for three layers; thin, intermediate and thick body. The result obtained for the two PPM was found to be comparable with negligible disparity.

CONCLUSION

In this study**,** the proton precession magnetometer was fabricated with high resolution sensor of inductance 55.4mH, a polarising current of about 0.48A for 12V supply and a RMS signal amplitude of 0.54µV. The signal to noise ratio (SNR) for bandwidth of 250 Hz is estimated as 61DB maximum, while the resonant capacitor for a precession frequency of 1715Hz equal to 0.8µF. The PPM sensor and processing unit were housed in two impact resistance plastic case. It has a total weight of 6kg and configured with external sound card of a laptop computer to digitized and analysed the resulting data using a software package called Spectrum Lab. Permanent noise peaks picked up by the sensor were visible as stripes on the scope displayed. The geomagnetic field value was determined via the Larmour relation $B_o = 23.496241 \times f$.

From the measurements carried out using the standard and locally fabricated proton precession magnetometer (PPM) and from the analysis of the results, it can be concluded that the local PPM, was found to be reliable for measuring the earth magnetic field with sufficient precision for the study of diurnal variation. However, for studies of geomagnetic micro pulsations, the precision needs to be improved further. In order to make more portable instrument, the digital signal processing component will have to be developed in an embedded system (microcontroller).

REFERENCES

1.TELFORD, W.M., GELDART, L.P. & SHERIFF, R.E. (1990). *Applied Geophysics*. Cambridge University Press, Cambridge, UK, 770 pp.

2.UMEGO, M.N. & OJO, S. B. (1995). A magnetic depth to basement analysis in the Sokoto basin, North Western Nigeria. *Journal of Mining and Geology*, **31**(2): 161–167.

3.YOUNG, C.T. & DROEGE, D.R. (1986). Archaeological applications of resistivity and magnetic methods at Fort Wilkins state park, Michigan. *Geophysics*, **51**(3): 568–575.

4.LOWRIE, W. (2011). *Fundamentals of Geophysics*. Cambridge University Press, Cambridge, UK, 381 pp.

5.OBOT, V.D. & WOLFE, P.J. (1981). Ground level magnetic study of Greene County, Ohio. *Ohio Journal of Science*, **80**:50–54.

6. RAHAMAN, M.A. (1976). Review of the basement Geology of Southwestern Nigeria. In: C.A. Kogbe, (Ed.). *Geology of Nigeria.* Elizabethan, Lagos, Nigeria. pp. 41–58.

7. KOEFOED, O. (1979). *Geosounding Principles*. Elsevier Science Publication, Amsterdam, Netherlands, 276 pp.

8. ISHOLA, K.S., ADEOTI, L. & OBIANERI, A. (2010). Interpretation of the historic site, Agorin in Badagry, Southwestern Nigeria using geophysical methods. *Ozean Journal of Applied Sciences*, **5** (1): 85–99.

9. KAYODE, J.S., NYABESE, P. & ADELUSI, A.O. (2010). Ground magnetic study of Ilesa east, Southwestern Nigeria. *African Journal of Environmental Science and Technology*, **4**(3):122–131.

10. KOHLER, J.A. (2004). *Proton Precession Magnetometer.* Comox, Canada, 27 pp.

11. KANNANGARA, M.L.T.& FERNANDO, P.C.B. (1969). Night time Equatorial Pi2Micropulsations. *Journal of Geophysical Research Space Physics*, **74**(3): 124-130.

12. OKUNLOLA, O.A. & SOMORIN, E.B. (2006). Compositional features of Precambrian pegmatite of Itakpe area, Central Nigeria. *Global Journal of Geological Science*, **4**(2): 221–230.

13. OKUNLOLA, O.A. & JIMBA, S. (2006). Compositional trends in relation to Ta-Nb mineralization in Precambrian pegmatite's of Aramoko-Ara-Ijero area, Southwestern Nigeria. *Journal of Mining and Geology*, **42**(2): 113–126.

14. OBAJE, N.G. (2009). *Geology and Mineral Resources of Nigeria*. Volume 120 of Lecture Notes in Earth Sciences, Berlin, Springer, New York, USA, 221 pp.

15. OJO AKINTAYO, O. (2013). Geomagnetic and geoelectric investigation of mineral rocks at Awo, Osun State, southwest Nigeria. *International Journal of Physical Research*, **1**(2):60–74.

16. GARBA, I. (2003). Geochemical discrimination of newly discovered rare metal bearing and barren pegmatite's in the Pan-African (600 ± 150 Ma) basement of northern Nigeria. *Transactions of the Institution of Mining and Metallurgy B: Applied Earth Science*, **112**(3): 287–292.

17. BAYOT, W. (2005). Practical *guidelines for building a magnetometer by hobbyists*. Introduction to magnetometer technology. 45 pp.

18. BREINER, S. (1999). *Application Manual for Portable Magnetometers*. Geometrics, San Jose California, USA.

19. KAYODE, J.S. & ADELUSI, A.O. (2010). Ground magnetic data interpretation of Ijebu-Jesa area, Southwestern Nigeria, using total component. *Research Journal of Applied Sciences, Engineering and Technology*, **2**(8): 703–709.

20. BUTLER, D.K. (2005). Near Surface Geophysics Textbook. *Society of Exploration Geophysics*, **13**: 240.

21. FOLAMI, S. L. (1992). Interpretation of aeromagnetic anomalies in Iwaraja area, South Western Nigeria. *Journal of Mining and Geology*, **28**(2): 393–397.

22. ROY, A (1972). Depth of investigation in Wenner, three-electrode and dipole-dipole DC resistivity methods. *Geophysical Prospecting*, **20**(2):329–340.

23. PHILIP, K., BROOKS, M. & HILL, L. (2002). *An Introduction to Geophysical Exploration*. Blackwell Science, London, UK, 262 pp.

24. ONI, R. & EBUN, B. (1969). Measurement and Interpretation of magnetic anomaly components in Low latitude. *Journal of geophysical Research*, **74**(17): 4233–4245.

25. OKUNLOLA, O.A., ADEIGBE, O.C. & OLUWATOKE, O.O. (2009). Compositional and petrogenetic features of schistose rocks of Ibadan area, Southwestern Nigeria. *Earth Sciences Research Journal*, **13**(2): 119–133.

26. NETTLETON, L.L. (1976). Gravity and Magnetic in Oil Prospecting. McGraw-Hill, New York, USA, 464 pp.

27. ADEKOYA, J.A. KEHINDE-PHILLIPS, O.O. & ODUKOYA, A.M. (2003). Geological distribution of mineral resources in Southwestern Nigeria. In: A.A. Elueze, (Ed.). *Prospects for Investment in Mineral Resourcesof Southwestern Nigeria*, Nigerian Mining and Geosciences (NMGS), pp. 1–13.

28. OKUNLOLA, O.A. & OGEDENGBE, O. (2003). Investment potential of gemstone occurrences in Southwestern

Nigeria. In: A.A. Elueze, (Ed.). *Prospects for Investment in Mineral Resources of Southwestern Nigeria*. Nigerian Mining and Geosciences Society (NMGS), pp. 41–45.

29. THOMPSON, R. & OLDFIELD, F. (1986). *Environment Magnetism*. Allen and Unwin, London, UK, 227 pp.
30. RUHUNUSIRI, W.D.S. & JAYANANDA, M.K. (2008). Construction of proton magnetometer. *Institute of physics – Sri Lanka*, **24**:78-85.
31. SEARLE, R.C. (2008). Magnetic susceptibility as a tool for investigating igneous rocks experience from IODP Expedition 304. *Scientific Drilling*, **6**:52–54.
32. PARASNIS, D.S. (1978). *Principles of Applied geophysics.* Chapman & Hall, New York, USA, 236 pp.
33. PETERS, L.J. (1949). The direct approach to magnetic interpretation and its practical application. *Geophysics*, **14**: 290–320.
34. RASTOGI, R.G., KITAMURA, T. & KITAMURA, K. (2004). First observations of geomagnetic field variations within equatorial electrojet belt in Sri-Lanka. *Indian Journal of Radio and Space Physics*, **33**:83-87.
35. OGUNSANWO, F.O., OLURIN, O.T., OZEBO, V.C., GANIYU, S.A., AYANDA, J.D., OGUNSANWO, B.T., OLOWOFELA, J.A., OKEYODE, I.C. & MUSTAPHA, O.A. (2022). Application of Enhancement and Filtering technique to Aeroradiometric data of Ogun State, South-Western, Nigeria, *Journal of Mining and Geology*, **58**(1): 63-73.